





**Third-order topological insulator in three-dimensional lattice of magnetic vortices**Z.-X. Li , Zhenyu Wang , Zhizhi Zhang , Yunshan Cao, and Peng Yan \**School of Electronic Science and Engineering and State Key Laboratory of Electronic Thin Films and Integrated Devices, University of Electronic Science and Technology of China, Chengdu 610054, China*

(Received 4 March 2021; accepted 11 June 2021; published 24 June 2021)

Recent acoustic and electrical-circuit experiments have reported the third-order (or octupole) topological insulating phase, while its counterpart in classical magnetic systems has yet to be realized. Here we explore the collective dynamics of magnetic vortices in three-dimensional breathing cuboids and find that the vortex lattice can support zero-dimensional corner states, one-dimensional hinge states, two-dimensional surface states, and three-dimensional bulk states when the ratio of alternating intralayer and interlayer bond lengths goes beyond a critical value. We show that only the corner states are stable against external frustrations because of the topological protection. Full micromagnetic simulations verify our theoretical predictions with good agreement.

DOI: [10.1103/PhysRevB.103.214442](https://doi.org/10.1103/PhysRevB.103.214442)**I. INTRODUCTION**

The recent discovery of higher-order topological insulators (HOTIs) [1–22] has extensively broadened our understanding of the topological phases of matter. The peculiar hinge and corner states emerging in HOTIs are attracting a lot of attention for both the fundamental interest (e.g., bulk-boundary correspondence) and the potential application in topological devices. In an  $n$ -dimensional system, the conventional topological insulator (TI), dubbed the first-order topological insulator (FOTI), supports  $(n - 1)$ -dimensional topological edge states [23,24], while the HOTI allows  $(n - k)$ -dimensional ( $2 \leq k \leq n$ ) topological bound states [25–32]. Presently, most HOTI states reported in the literature belong to the second-order phase ( $k = 2$ ), with a few exceptions of third-order TIs ( $k = 3$ ) being realized in acoustic and electric-circuit experiments. The main difficulty lies in the fabrication and detection of the rather spatially localized corner state in three-dimensional devices, while the artificial crystal can well overcome this issue.

Recently, the topological states in classical magnetic systems have received much interest from the spintronics community. Both the first- [33–40] and second-order [41–44] topological phases of the spin wave, one of the elementary excitations in ordered magnets, have been studied. In addition, topological insulating states emerging in metamaterials based on magnetic solitons (such as domain wall, vortex, and skyrmion) [45–49] are attracting growing interest as well. Kim and Tserkovnyak [50] and Li *et al.* [51] showed that the two-dimensional honeycomb lattice of magnetic solitons can support robust chiral edge states. The realization of Su-Schrieffer-Heeger (SSH) [52] states in a one-dimensional magnetic soliton lattice was demonstrated very recently by Li *et al.* [53] and Go *et al.* [54]. Moreover, it has been

predicted that the second-order TI phases can appear in breathing kagome [55], honeycomb [56], and square [57] lattices of magnetic vortices under the proper conditions. A thorough review of topological insulators and semimetals in classical magnetic systems can be found in Ref. [58]. So far, all TI states reported in classical magnetic systems belong to the first- or second-order phase. The observation of the third-order phase is still lacking.

In this paper, we present both analytical and numerical studies of the collective dynamics of magnetic vortices arranged in a three-dimensional breathing cuboid lattice [see Fig. 1(a)]. By solving the equations of motion of interacting vortices, we obtain the band structures and predict that the third-order topological in-gap edge states (corner states) emerge when the geometric conditions  $d_1/d_2 > 1$  and  $h_1/h_2 > 1$  are satisfied simultaneously. Here  $d_1$  and  $d_2$  ( $h_1$  and  $h_2$ ) are the alternating lengths of intralayer (interlayer) intracellular and intercellular bonds, respectively, as shown in Figs. 1(b) and 1(c). Under such conditions, the one-dimensional hinge states, two-dimensional surface states, and three-dimensional bulk states are identified to be topologically trivial. These results can be understood in terms of the picture provided by the generalized SSH model. The robustness of the corner states is investigated by introducing moderate disorder and defects to this three-dimensional soliton system. We perform full micromagnetic simulations to verify theoretical predictions and find good agreement between them. It is noted that the fabrication [59,60] and orbit tracking [61] of the magnetic soliton lattice are within the reach of current technology. Our findings open a route toward realizing third-order TIs in classical magnetic systems that may inspire the design of robust spintronic devices in the future.

The outline of this paper is as follows: In Sec. II, we present the model and method. Topological phases of the three-dimensional vortex lattice are discussed in Sec. III, including theoretical calculations and micromagnetic

\*Corresponding author: yan@uestc.edu.cn

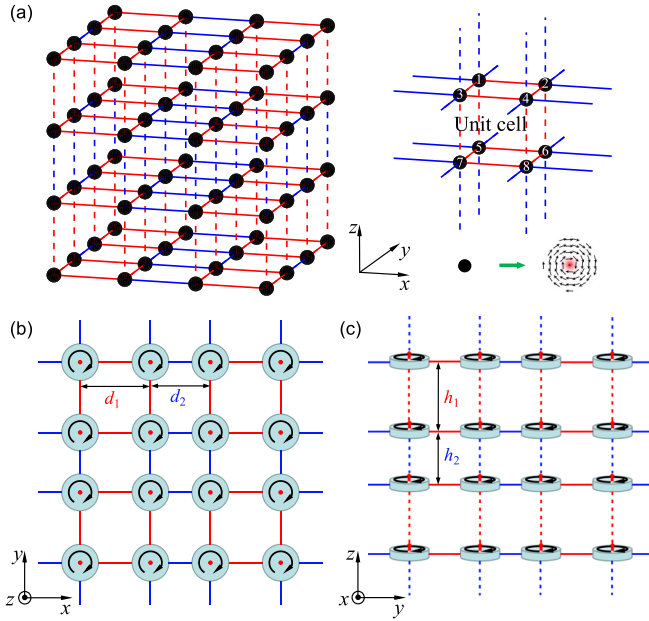


FIG. 1. (a) Illustration of a three-dimensional magnetic vortex lattice, with black balls denoting nanodisks with the vortex state and solid (dashed) red and blue segments representing alternating lengths of intralayer (interlayer) intracellular and intercellular bonds, respectively. (b) Top and (c) side views of the crystal structure.  $d_1$ ,  $d_2$ ,  $h_1$ , and  $h_2$  are the bond lengths.

simulations. Conclusions and the outlook are drawn in Sec. IV.

## II. MODEL AND METHOD

A three-dimensional breathing cuboid lattice of magnetic nanodisks with vortex states is considered, as shown in Fig. 1. The collective dynamics around the frequency of the gyrotropic vortex mode can be modeled by Thiele's equation [50,62]:

$$\mathcal{G}\hat{z} \times \frac{d\mathbf{U}_j}{dt} + \mathbf{F}_j = 0, \quad (1)$$

where  $\mathbf{U}_j = \mathbf{R}_j - \mathbf{R}_j^0$  is the displacement of the  $j$ th vortex core from the equilibrium position  $\mathbf{R}_j^0$  and  $\mathcal{G} = -4\pi QwM_s/\gamma$  is the gyroscopic constant, with  $Q = \frac{1}{4\pi} \iint dxdy \mathbf{m} \cdot (\frac{\partial \mathbf{m}}{\partial x} \times \frac{\partial \mathbf{m}}{\partial y})$  being the topological charge of the vortex state,  $\mathbf{m}$  being the unit vector along the local magnetization direction,  $w$  being the thickness of the nanodisk,  $M_s$  being the saturation magnetization, and  $\gamma$  being the gyromagnetic ratio.  $\mathbf{F}_j = -\partial \mathcal{W}/\partial \mathbf{U}_j$  is the conservative force, where  $\mathcal{W}$  is the total energy including both the confining potential on the vortex due to the nanodisk boundary and the (intralayer and interlayer) coupling between nearest-neighbor nanodisks:  $\mathcal{W} = \sum_j \mathcal{K}U_j^2/2 + \sum_{j \neq k} U_{jk}/2$ , with  $U_{jk} = \mathcal{I}_{\parallel}U_j^{\parallel}U_k^{\parallel} - \mathcal{I}_{\perp}U_j^{\perp}U_k^{\perp} + \mu\mathbf{U}_j \cdot \mathbf{U}_k$  [63–65]. Here  $\mathcal{K}$  is the spring constant,  $\mathcal{I}_{\parallel}$  ( $\mathcal{I}_{\perp}$ ) is the intralayer longitudinal (transverse) coupling constant, and  $\mu$  is the interlayer coupling parameter.

Imposing  $\mathbf{U}_j = (u_j, v_j)$  and defining  $\psi_j = u_j + iv_j$ , Eq. (1) can be rewritten as

$$\begin{aligned} -i\dot{\psi}_j &= \left( \omega_0 - \frac{\xi_1^2 + \xi_2^2}{\omega_0} \right) \psi_j + \sum_{k \in \langle j \rangle, l} \zeta_l \psi_k + \sum_{k \in \langle j' \rangle, n} \eta_n \psi_k \\ &- \frac{\xi_1 \xi_2}{2\omega_0} \sum_{s \in \langle \langle j_1 \rangle \rangle} e^{i2\bar{\theta}_{js}} \psi_s - \frac{\xi_2^2}{2\omega_0} \sum_{s \in \langle \langle j_2 \rangle \rangle} e^{i2\bar{\theta}_{js}} \psi_s \\ &- \frac{\xi_1^2}{2\omega_0} \sum_{s \in \langle \langle j_3 \rangle \rangle} e^{i2\bar{\theta}_{js}} \psi_s, \end{aligned} \quad (2)$$

where  $\omega_0 = \mathcal{K}/|\mathcal{G}|$ ,  $\zeta_l = (\mathcal{I}_{\parallel, l} - \mathcal{I}_{\perp, l})/2|\mathcal{G}|$ , and  $\xi_l = (\mathcal{I}_{\parallel, l} + \mathcal{I}_{\perp, l})/2|\mathcal{G}|$ , in which  $l = 1$  ( $l = 2$ ) represents the intralayer intracellular (intercellular) connection;  $\eta_n = \mu_n/|\mathcal{G}|$ , where  $n = 1$  ( $n = 2$ ) denotes the interlayer intracellular (intercellular) bond;  $\bar{\theta}_{js} = \theta_{jk} - \theta_{ks}$  is the relative angle from the bond  $k \rightarrow s$  to the bond  $j \rightarrow k$  with  $k$  between  $j$  and  $s$ ; and  $\langle j \rangle$  and  $\langle j' \rangle$  are the set of intralayer and interlayer nearest neighbors of  $j$ , respectively;  $\langle \langle j_1 \rangle \rangle$ ,  $\langle \langle j_2 \rangle \rangle$ , and  $\langle \langle j_3 \rangle \rangle$  represent the intralayer next-nearest neighbors of  $j$ .

To solve Eq. (2) numerically, the key parameters  $\mathcal{K}$ ,  $\mathcal{I}_{\parallel}$ ,  $\mathcal{I}_{\perp}$ , and  $\mu$  should be determined. First, the spring constant  $\mathcal{K}$  can be obtained from the relation  $\mathcal{K} = \omega_0|\mathcal{G}|$ , with  $\omega_0$  being the gyrotropic frequency of a single vortex. For a permalloy (Py) [66,67] nanodisk of the vortex state with thickness  $w = 10$  nm and radius  $r = 50$  nm, gyrotropic frequency  $\omega_0 = 2\pi \times 0.939$  GHz, and gyroscopic constant  $\mathcal{G} = -3.0725 \times 10^{-13}$  J s rad $^{-1}$  m $^{-2}$  ( $Q = 1/2$ ) [55], we have  $\mathcal{K} = 1.8128 \times 10^{-3}$  J m $^{-2}$ . Second, the analytical expressions of  $\mathcal{I}_{\parallel}$  and  $\mathcal{I}_{\perp}$  for the distance  $d$  between vortices have been obtained in a simplified two-nanodisk system [55]. Finally, the dependence of parameter  $\mu$  on the distance  $h$  can also be determined from micromagnetic simulations by considering a stacking two-vortex system (see Appendix A for details).

For an infinite three-dimensional vortex lattice, the unit cell can be selected as shown in Fig. 1(a). The three basis vectors of the system are  $\mathbf{a}_1 = (d_1 + d_2)\hat{x}$ ,  $\mathbf{a}_2 = (d_1 + d_2)\hat{y}$ , and  $\mathbf{a}_3 = (h_1 + h_2)\hat{z}$ . By performing a plane wave expansion of  $\psi_j$ , we obtain the matrix form of the Hamiltonian expressed in the momentum space:

$$\mathcal{H} = \begin{pmatrix} Q_0 & Q_1 & Q_2 & Q_3 & Q_4 & 0 & 0 & 0 \\ Q_1^* & Q_0 & Q_5 & Q_2 & 0 & Q_4 & 0 & 0 \\ Q_2^* & Q_5^* & Q_0 & Q_1 & 0 & 0 & Q_4 & 0 \\ Q_3^* & Q_2^* & Q_1^* & Q_0 & 0 & 0 & 0 & Q_4 \\ Q_4^* & 0 & 0 & 0 & Q_0 & Q_1 & Q_2 & Q_3 \\ 0 & Q_4^* & 0 & 0 & Q_1^* & Q_0 & Q_5 & Q_2 \\ 0 & 0 & Q_4^* & 0 & Q_2^* & Q_5^* & Q_0 & Q_1 \\ 0 & 0 & 0 & Q_4^* & Q_3^* & Q_2^* & Q_1^* & Q_0 \end{pmatrix}, \quad (3)$$

with the matrix elements

$$Q_0 = \omega_0 - \frac{\xi_1^2 + \xi_2^2}{\omega_0} - \frac{\xi_1 \xi_2}{\omega_0} [\cos(\mathbf{k} \cdot \mathbf{a}_1) + \cos(\mathbf{k} \cdot \mathbf{a}_2)],$$

$$Q_1 = \zeta_1 + \zeta_2 \exp(-i\mathbf{k} \cdot \mathbf{a}_1),$$

$$Q_2 = \zeta_1 + \zeta_2 \exp(i\mathbf{k} \cdot \mathbf{a}_2),$$

$$Q_3 = \frac{\xi_1 \xi_2}{\omega_0} [\exp(i\mathbf{k} \cdot \mathbf{a}_2) + \exp(-i\mathbf{k} \cdot \mathbf{a}_1)]$$

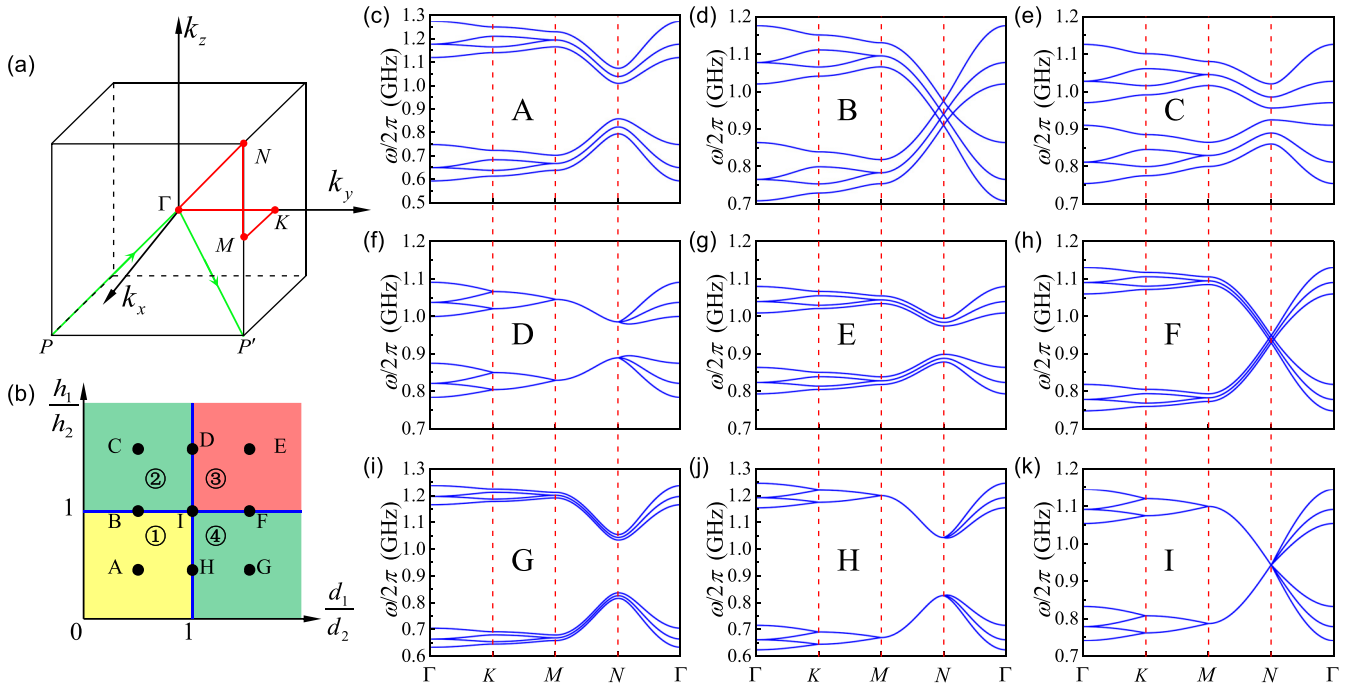


FIG. 2. (a) The first Brillouin zone, with the high-symmetry points  $\Gamma$ ,  $K$ ,  $M$ , and  $N$  locating at  $(k_x, k_y, k_z) = (0, 0, 0)$ ,  $(0, \frac{\pi}{d_1+d_2}, 0)$ ,  $(\frac{\pi}{d_1+d_2}, \frac{\pi}{d_1+d_2}, 0)$ , and  $(\frac{\pi}{d_1+d_2}, \frac{\pi}{d_1+d_2}, \frac{\pi}{h_1+h_2})$ , respectively. (b) The phase diagram of the system, with  $d_2$  and  $h_2$  being fixed to 150 and 70 nm, respectively. (c)–(k) The band structures along the path  $\Gamma$ - $K$ - $M$ - $N$ - $\Gamma$  for different geometric parameters ( $d_1$  and  $h_1$ ) as marked by black dots in (b).

$$\begin{aligned}
 & + \frac{\xi_2^2}{\omega_0} \exp[i\mathbf{k} \cdot (\mathbf{a}_2 - \mathbf{a}_1)] + \frac{\xi_1^2}{\omega_0}, \\
 Q_4 &= \eta_1 + \eta_2 \exp(i\mathbf{k} \cdot \mathbf{a}_3), \\
 Q_5 &= \frac{\xi_1 \xi_2}{\omega_0} [\exp(i\mathbf{k} \cdot \mathbf{a}_2) + \exp(i\mathbf{k} \cdot \mathbf{a}_1)] \\
 & + \frac{\xi_2^2}{\omega_0} \exp[i\mathbf{k} \cdot (\mathbf{a}_2 + \mathbf{a}_1)] + \frac{\xi_1^2}{\omega_0}, \quad (4)
 \end{aligned}$$

where  $\mathbf{k}$  is the wave vector.

The spectrum of Hamiltonian (3) fully determines the phase allowed in a finite crystal due to the principle of bulk-boundary correspondence. In what follows, we present detailed calculations and discussions.

### III. THIRD-ORDER TOPOLOGICAL INSULATOR

#### A. Theoretical calculations

First, we calculate the bulk band structure along the path  $\Gamma$ - $K$ - $M$ - $N$ - $\Gamma$  in the first Brillouin zone [see Fig. 2(a)] for different geometric parameters, as shown in Figs. 2(c)–2(k), with the parameters  $d_2$  and  $h_2$  being fixed to 150 and 70 nm, respectively. One can see that the system supports eight bands due to the interlayer coupling between nanodisks, in contrast to the four-band structure in a two-dimensional breathing square vortex lattice obtained in Ref. [57]. Generally speaking, the energy degeneracy is often associated with some symmetry. A gap opening is usually caused by a symmetry breaking. For parameters  $(d_1, h_1) = (150 \text{ nm}, 70 \text{ nm})$ , labeled I in Fig. 2(b), we can see that all bands merge together, leading to a gapless band structure, as shown in Fig. 2(k). Here the system

respects the inversion symmetry. On the one hand, if we keep  $d_1/d_2 = 1$  and let  $h_1/h_2 \neq 1$ , the inversion symmetry along the  $z$ -axis direction is broken; then the band gap will open at high-symmetry point  $N$  [see Figs. 2(f) and 2(j)], where D and H represent parameters  $(d_1, h_1) = (150 \text{ nm}, 110 \text{ nm})$  and  $(150 \text{ nm}, 40 \text{ nm})$ , respectively. On the other hand, if we keep  $h_1/h_2 = 1$  while letting  $d_1/d_2 \neq 1$ , the inversion symmetry along the  $x$ -axis and  $y$ -axis directions is broken; then the band gaps open at high-symmetry points  $K$  and  $M$  [see Figs. 2(d) and 2(h)], with B and F representing parameters  $(d_1, h_1) = (120 \text{ nm}, 70 \text{ nm})$  and  $(180 \text{ nm}, 70 \text{ nm})$ , respectively. Finally, if  $d_1/d_2 \neq 1$  and  $h_1/h_2 \neq 1$ , the inversion symmetry along three directions ( $x$ -axis,  $y$ -axis, and  $z$ -axis directions) is broken, and the band gaps open at all high-symmetry points ( $K$ ,  $M$ , and  $N$ ), as shown in Figs. 2(c), 2(e), 2(g), and 2(i), with the parameters  $(d_1, h_1) = (120 \text{ nm}, 40 \text{ nm})$ ,  $(120 \text{ nm}, 110 \text{ nm})$ ,  $(180 \text{ nm}, 110 \text{ nm})$ , and  $(180 \text{ nm}, 40 \text{ nm})$ , respectively. We therefore conclude that the lifted degeneracy at the high-symmetry points is the result of the inversion symmetry breaking. To further distinguish whether these insulating phases are topologically protected, one should study the eigenmodes in finite systems and their robustness.

To find the higher-order topological edge states, we calculate the eigenfrequencies of a finite system with 512 ( $8 \times 8 \times 8$ ) nanodisks for four different parameter regions [see Fig. 2(b)]. For region 1, we set  $(d_1, d_2, h_1, h_2) = (104 \text{ nm}, 180 \text{ nm}, 40 \text{ nm}, 110 \text{ nm})$ , with the eigenfrequencies of the system shown in Fig. 3(a). By analyzing the spatial distribution of the wave function, we identify that the system can support only the bulk states [see Fig. 3(h)]. Then we consider region 2, with the geometric parameters  $(d_1, d_2, h_1, h_2) = (104 \text{ nm}, 180 \text{ nm}, 110 \text{ nm}, 40 \text{ nm})$ , and the eigenfrequencies are shown

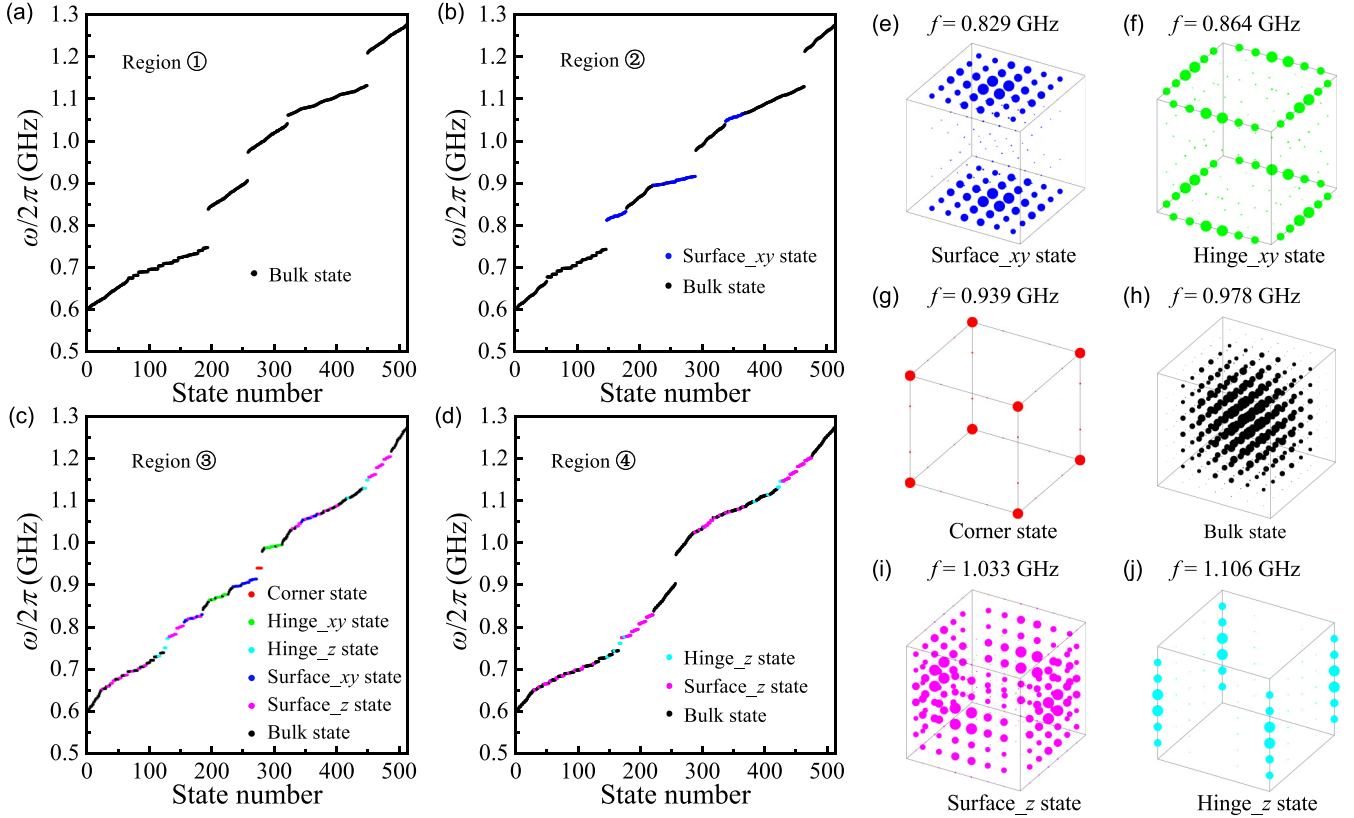


FIG. 3. Eigenfrequencies of the collective vortex gyration in a three-dimensional  $8 \times 8 \times 8$  system for (a) parametric region 1, (b) parametric region 2, (c) parametric region 3, and (d) parametric region 4, as marked in Fig. 2(b). (e)–(j) The spatial distribution of different modes. Here the size of the colorful balls is proportional to the amplitude of the wave function.

in Fig. 3(b), from which one can see that the system can support both the surface  $xy$  states and the bulk states, with the spatial distribution of the surface  $xy$  states plotted in Fig. 3(e). For region 3, we set  $(d_1, d_2, h_1, h_2) = (180 \text{ nm}, 104 \text{ nm}, 110 \text{ nm}, 40 \text{ nm})$ , and the spectrum is plotted in Fig. 3(c). One can clearly see that five different edge states emerge, including the zero-dimensional corner states [see Fig. 3(g)], two one-dimensional hinge states [see Figs. 3(f) and 3(j)], and two two-dimensional surface states [see Figs. 3(e) and 3(i)]. Finally, for region 4, we set parameters  $(d_1, d_2, h_1, h_2) = (180 \text{ nm}, 104 \text{ nm}, 40 \text{ nm}, 110 \text{ nm})$ . In this case, we observe the hinge  $z$ , surface  $z$ , and bulk states [see Figs. 3(j), 3(i), and 3(h)].

To judge whether the emerging edge states in Fig. 3(c) are topologically protected, we calculate the spectrum of the system in the presence of disorder and defects (see Appendix B for details). We find that only the corner states are topologically stable, while other edge modes (hinge and surface states) are trivial and sensitive to the introduced disturbances. We therefore realize the third-order TI in a classical magnetic system based on vortex metamaterials. These results can be straightforwardly understood by the SSH model. On the one hand, as shown in Ref. [57], we have proved that a two-dimensional breathing square lattice of vortices can support a second-order topological edge state when  $d_1/d_2 > 1$ . On the other hand, the layered structure can be viewed as a one-dimensional analog of the SSH model. In addition, the number (8) of layers is even. Therefore, only when  $h_1/h_2 > 1$

can the system support topological edge state [53]. We thus conclude that the third-order topological insulating phase can appear if and only if the geometric conditions  $d_1/d_2 > 1$  and  $h_1/h_2 > 1$  are satisfied simultaneously. It is worth mentioning that, if the number of layers is odd, the geometric conditions for the emergence of topological corner states are  $d_1/d_2 > 1$  and  $h_1 \neq h_2$ . Interestingly, in this case, the corner states will appear in either the upper or lower surface depending on the value of  $h_1/h_2 > 1$  and  $h_1/h_2 < 1$ , respectively.

Moreover, the topologically invariant  $\mathbb{Z}_4$  Berry phase can be used to characterize the HOTI state [56–58]:

$$\theta = \int_{L_1} \left[ i\Psi^\dagger(\mathbf{k}) \frac{\partial}{\partial \mathbf{k}} \Psi(\mathbf{k}) \right] \cdot d\mathbf{k} \pmod{2\pi}, \quad (5)$$

where  $\Psi(\mathbf{k})$  is the eigenvector for the band closest to the frequency of corner states.  $L_1$  is an integral path in the momentum space [see the green line segment in Fig. 2(a)]. Then we can find that the  $\mathbb{Z}_4$  Berry phase is quantized to zero in region 1 and to  $\pi$  in region 3, which indicates that these two regions represent two topologically distinct phases.

## B. Micromagnetic simulations

To confirm the theoretical predictions above, we perform full micromagnetic simulations. All material parameters adopted in the simulations are the same as those in the theoretical calculations presented in Fig. 3(c), with the saturation magnetization  $M_s = 0.86 \times 10^6 \text{ A/m}$ , the exchange

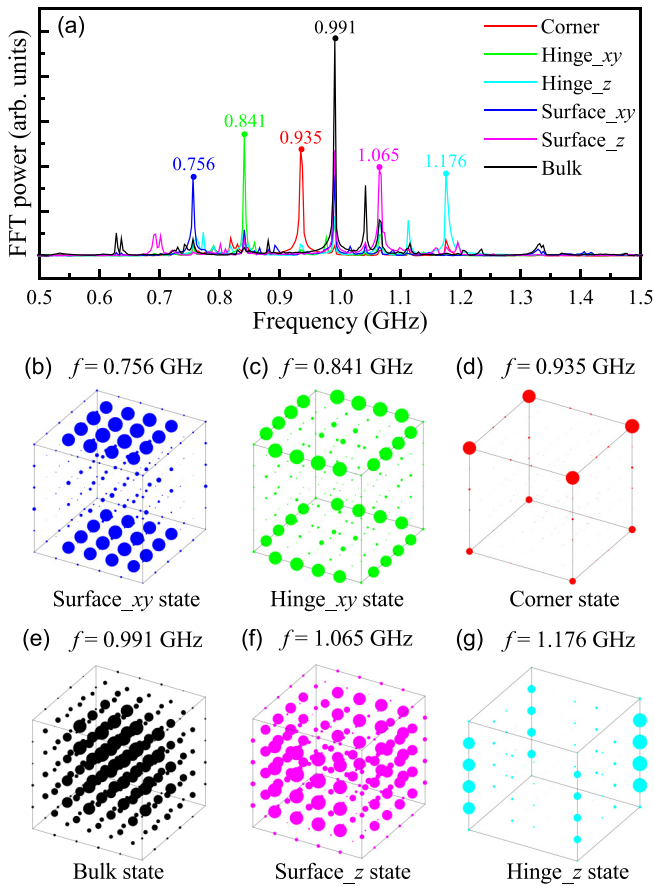


FIG. 4. (a) The temporal Fourier spectra of the vortex oscillations at different positions. Here the exciting field is applied to the whole system. (b)–(g) The spatial distribution of FFT intensity with different frequencies as marked in (a). The size of the balls reflects the strength of the oscillation.

stiffness  $A = 1.3 \times 10^{-11}$  J/m, and the Gilbert damping constant  $\alpha = 10^{-4}$ . To reduce the computational workload, we consider the  $6 \times 6 \times 6$  nanodisk system in the simulation. The micromagnetic package MUMAX3 [68] is used to simulate the collective dynamics of the vortex lattice. Here the cell size is set to  $2 \times 2 \times 10$  nm<sup>3</sup>. A sinc-function magnetic field  $H(t) = H_0 \sin[2\pi f(t - t_0)]/[2\pi f(t - t_0)]$  along the  $x$  direction with  $H_0 = 10$  mT,  $f = 30$  GHz, and  $t_0 = 1$  ns is applied to the whole system for 352 ns. Then the full spectrum of the system can be obtained by analyzing the collective oscillation of the vortex lattice. The positions of vortex cores  $\mathbf{R}_j = (R_{j,x}, R_{j,y})$  in all nanodisks are recorded every 200 ps. Here  $R_{j,x} = \frac{\iint x|m_z|^2 dx dy}{\iint |m_z|^2 dx dy}$ , and  $R_{j,y} = \frac{\iint y|m_z|^2 dx dy}{\iint |m_z|^2 dx dy}$ , with the integral region confined in the  $j$ th nanodisk. The temporal fast Fourier transform (FFT) spectra of the vortex oscillations at different positions are plotted in Fig. 4(a). Here the red, green, cyan, blue, magenta, and black curves denote the positions of corner, hinge  $xy$ , hinge  $z$ , surface  $xy$ , surface  $z$ , and bulk bands, respectively. From Fig. 4(a), one can clearly identify the frequency range supporting different modes. To visualize the spatial distribution of vortex oscillation for different modes, we plot the spatial distribution of the FFT intensity with six representative frequencies [see Fig. 4(a)], as shown

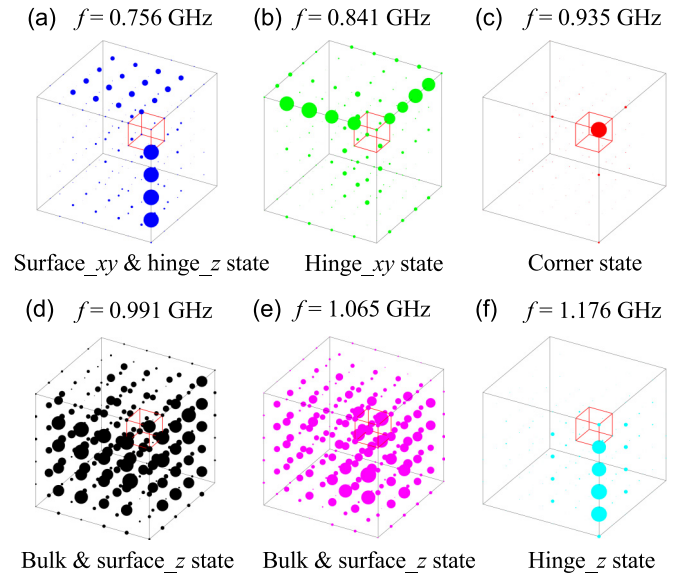


FIG. 5. The spatial distribution of vortex oscillations under the local exciting field with different frequencies.

in Figs. 4(b)–4(g). Here the radius of the balls is proportional to the FFT strength. We identify the following modes: (i) a surface  $xy$  state with oscillation localized at the top and bottom surfaces [see Fig. 4(b)], (ii) a hinge  $xy$  state with oscillation localized at the eight edges of the top and bottom surfaces [see Fig. 4(c)], (iii) a corner state with oscillation localized at eight corners [see Fig. 4(d)], (iv) a bulk state with oscillation spread over the system except the surfaces [see Fig. 4(e)], (v) a surface  $z$  state with oscillation localized at four side surfaces [see Fig. 4(f)], and (vi) a hinge  $z$  state with oscillation localized at four side edges [see Fig. 4(g)]. These results agree well with theoretical calculations.

In the above simulations, the external driving source (of the sinc function) is applied over the whole lattice, which prevents us from observing the time evolution of each mode. Here we stimulate the collective vortex dynamics by applying a sinusoidal magnetic field  $\mathbf{h}(t) = h_0 \sin(2\pi ft)\hat{x}$ , with  $h_0 = 0.01$  mT and  $t = 60$  ns, localized at eight nanodisks at one corner, as denoted by red cubes in Fig. 5. For different frequencies, we plot the spatial distribution of vortex oscillations, as shown in Figs. 5(a)–5(f), with the size of the balls representing the amplitude of the vortex oscillations. We can clearly see that the spatial distribution of the hinge  $xy$  state, corner state, and hinge  $z$  state compare well with the corresponding modes plotted in Fig. 4, while the other three modes do not. Interestingly, we observe various hybridized modes, including a surface  $xy$  and hinge  $z$  state [Fig. 5(a)] and a bulk and surface  $z$  state [Figs. 5(d) and 5(e)]. The reason for the mode hybridization is that the frequencies of these states are close and their wave functions have significant overlap (see Fig. 4). In addition, one can clearly see that the hinge  $xy$  states are not chiral from Fig. 5(b). However, we cannot identify whether the vertical hinge states (hinge  $z$  state) are chiral. To resolve this issue, we apply a driving magnetic field to a bottom corner of the sample with  $f = 1.176$  GHz, and we find that the vertical hinge states are excited as well (not

shown here). We therefore conclude that all hinge states are actually not chiral.

#### IV. DISCUSSION AND CONCLUSION

In this work, we predicted the third-order TI in a three-dimensional (3D) magnetic system for the first time. The generalization from two to three dimensions is not trivial at all. From the analytical aspect, the form of the interlayer coupling as a function of the distance is fundamentally different from that of the in-plane distance: First, it is isotropic instead of being anisotropic. Second, it follows an inverse relation ( $1/d$ ) [69,70], rather than an inverse cube law ( $1/d^3$ ) [55–57]. From the numerical aspect, the full micromagnetic simulation of a 3D vortex lattice consumes (10 times) more computational time than a two-dimensional (2D) one even if the number of nanodisks is the same. The 3D vortex crystal exhibits more abundant physics than the 2D system. For example, the one-dimensional hinge state reported in this work can serve as the building block to construct a 3D magnonic waveguide when the vortex crystal is properly cut and/or spliced, in contrast to conventional 2D magnon waveguides constructed by either magnetic nanowires [71–75] or magnetic domain walls [76–78].

It is worth noting that in our previous works [55–57], the higher-order terms are considered in Thiele’s equation to capture the higher-frequency ( $\sim 10$  GHz) behavior of the magnetic vortices. However, in this paper, we aimed to predict the existence of the third-order topological insulating phase in the vortex lattice and focused on its low-frequency behaviors (subgigahertz). Therefore, for simplicity, we ignored both the inertial and non-Newtonian effects. Of course, if we included the higher-order terms in our model, we would obtain three bands around 0.939, 11.945, and 14.192 GHz (which can be straightforwardly done but is not shown here), around which one will observe two extra 3D TI states with higher frequencies ( $\sim 10$  GHz).

To conclude, we studied the third-order TI in a three-dimensional breathing cuboid lattice of magnetic vortices. The geometric condition to observe this phase was analyzed by the SSH model. We showed that the third-order corner states are robust against moderate disorder and defects. Full micromagnetic simulations were implemented to verify theoretical predictions with great agreement. Our findings pave the way for realizing a third-order TI in classical magnetic systems, which should have potential applications for designing robust spintronics devices. In this work, we have assumed that the polarity and chirality of all vortices are identical; the effect of different polarities and chiralities on the higher-order topology is an interesting topic for future research.

#### ACKNOWLEDGMENTS

This work was supported by the National Natural Science Foundation of China (NSFC; Grants No. 12074057, No. 11604041, and No. 11704060). Z.-X.L. acknowledges financial support from the China Postdoctoral Science Foundation (Grant No. 2019M663461) and the NSFC (Grant No. 11904048). Z.W. was supported by the China Postdoctoral Science Foundation under Grant No. 2019M653063. Z.Z.

acknowledges the support from the China Postdoctoral Science Foundation under Grant No. 2020M673180.

#### APPENDIX A: THE DETERMINATION OF INTERLAYER COUPLING PARAMETER

The interlayer coupling parameter  $\mu$  is very important for solving the dynamical equation of vortex motion. Here we determine this parameter by considering the dynamics of a two-nanodisk system with the vortex state, as shown in Fig. 6(a). For such a case, the potential energy can be expressed as  $\mathcal{W} = \sum_j \mathcal{K} \mathbf{U}_j^2 / 2 + \sum_{j \neq k} \mu \mathbf{U}_j \cdot \mathbf{U}_k / 2$ . By imposing  $\psi_j = u_j + iv_j$  and  $\psi_j = \psi_j e^{i\omega t}$ , the dynamical equations for the two-vortex system can be simplified to

$$\omega \psi_1 = \frac{\mathcal{K}}{|\mathcal{G}|} \psi_1 + \frac{\mu}{|\mathcal{G}|} \psi_2, \quad \omega \psi_2 = \frac{\mathcal{K}}{|\mathcal{G}|} \psi_2 + \frac{\mu}{|\mathcal{G}|} \psi_1. \quad (\text{A1})$$

By solving Eq. (A1), we can obtain two resonant frequencies:  $\omega_1 = (\mathcal{K} - \mu)/|\mathcal{G}|$  and  $\omega_2 = (\mathcal{K} + \mu)/|\mathcal{G}|$ . Therefore, the interlayer coupling parameter  $\mu$  can be expressed as  $\mu = (\omega_2 - \omega_1)|\mathcal{G}|/2$ . Figure 6(b) plots the Fourier spectrum of the vortex oscillation for  $h = 70$  nm. The frequencies of the peaks read  $\omega_1/2\pi = 0.863$  GHz and  $\omega_2/2\pi = 1.019$  GHz; then we obtain  $\mu = 1.5058 \times 10^{-4}$  J m $^{-2}$ . Similarly, we can get the frequencies of the two-vortex system by varying  $h$ . Figure 6(c) plots the  $h$  dependence of  $\omega_1$  and  $\omega_2$ . It shows that, with the increase of  $h$ ,  $\omega_1$  increases, while  $\omega_2$  decreases. One naturally expects  $\omega_1 = \omega_2 = \omega_0$  when  $d \rightarrow \infty$ . The dipole interaction between two vortices can be simplified as the interaction between magnetic charges of the vortex cores [69,70],

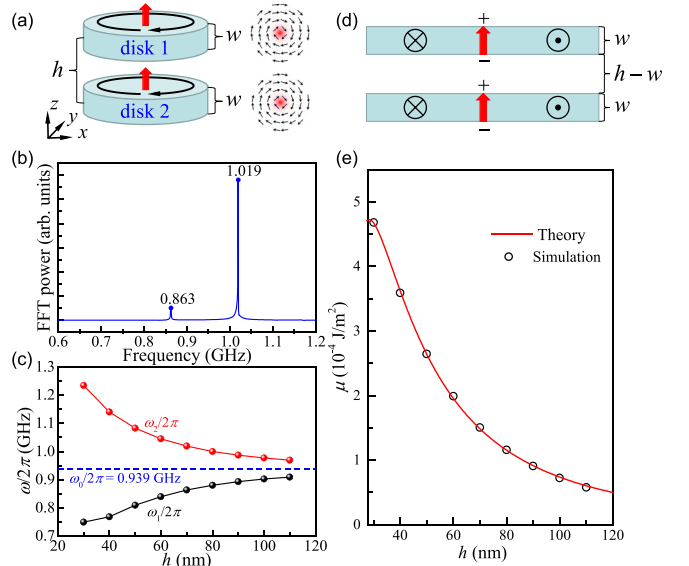


FIG. 6. (a) Schematic plot of the stacking two-vortex system. The micromagnetic structures of vortices are also shown. (b) The Fourier spectrum of the vortex oscillation for  $h = 70$  nm. (c) The two eigenfrequencies of the two-vortex system varying with  $h$ . (d) The illustration of the interaction between magnetic charges. (e) Dependence of the interlayer coupling parameter  $\mu$  on  $h$ . Black circles denote simulation results, and the red solid line represents the analytical formula.

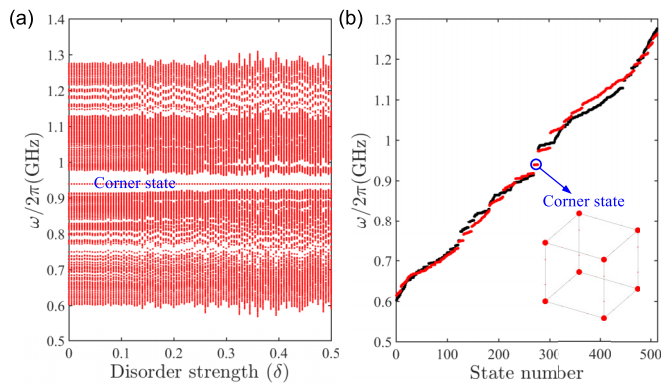


FIG. 7. (a) Eigenfrequencies of the three-dimensional vortex lattice under different disorder strengths. (b) Eigenfrequencies of the three-dimensional vortex lattice in the absence of defects (black balls) and in the presence of defects (red balls). The blue circle indicates the topologically stable corner state, with the inset showing the corresponding spatial distribution. The results presented in both (a) and (b) are obtained by the exact diagonalization of an  $8 \times 8 \times 8$  (512 nanodisks) finite system.

as illustrated in Fig. 6(d). Further, the interaction between magnetic charges can be divided into three parts: (i) the attractive interaction between the negative magnetic charge of disk 1 and positive magnetic charge of disk 2 [ $\propto 1/(h-w)$ ], (ii) the repulsive interaction of the same magnetic charge between disk 1 and disk 2 ( $\propto 1/h$ ), and (iii) the attractive interaction between the positive magnetic charge of disk 1 and

negative magnetic charge of disk 2 [ $\propto 1/(h+w)$ ]. To obtain the analytical expression of  $\mu$  on  $h$ , we use  $c_1/(h-w) + c_2/h + c_3/(h+w)$  to fit the simulation results. The curve in Fig. 6(e) shows the best fit of the numerical date with  $c_1 = -5.7478 \times 10^{-11} \text{ J m}^{-1}$ ,  $c_2 = 2.3695 \times 10^{-10} \text{ J m}^{-1}$ , and  $c_3 = -1.8229 \times 10^{-10} \text{ J m}^{-1}$ .

## APPENDIX B: THE ROBUSTNESS OF THIRD-ORDER TOPOLOGICAL EDGE STATES

To verify the topological nature of the corner states emerging in Fig. 3, we calculate the eigenfrequencies of the three-dimensional vortex lattice with disorder and defects. The numerical results are presented in Figs. 7(a) and 7(b). Here the disorder is introduced to all vortices by assuming the interlayer coupling parameter  $\mu$  undergoing a random variation:  $\mu \rightarrow \mu(1 + \delta Z)$ , where  $\delta$  is the strength of the disorder and  $Z$  is a uniformly distributed random number between  $-1$  and  $1$ . The defects are introduced to some vortices (the nanodisks in the second, fourth and sixth rows of each layer) by assuming a shift in the coupling parameters  $\zeta$ ,  $\xi$ , and  $\mu$ :  $\zeta \rightarrow 0.8\zeta$ ,  $\xi \rightarrow 0.8\xi$ , and  $\mu \rightarrow 1.2\mu$ . From Fig. 7(a), one can clearly see that with the increasing of the disorder strength, the corner state is very robust. Meanwhile, when defects are included, the frequency of the corner state is perfectly pinned to 0.939 GHz, while the frequencies of hinge, surface, and bulk states are significantly modified [see Fig. 7(b)]. These results thus support the conclusion that the third-order corner states emerging in our system are topologically stable.

- [1] W. A. Benalcazar, B. A. Bernevig, and T. L. Hughes, Quantized electric multipole insulators, *Science* **357**, 61 (2017).
- [2] W. A. Benalcazar, B. A. Bernevig, and T. L. Hughes, Electric multipole moments, topological multipole moment pumping, and chiral hinge states in crystalline insulators, *Phys. Rev. B* **96**, 245115 (2017).
- [3] M. Ezawa, Higher-Order Topological Insulators and Semimetals on the Breathing Kagome and Pyrochlore Lattices, *Phys. Rev. Lett.* **120**, 026801 (2018).
- [4] Z. Song, Z. Fang, and C. Fang,  $(d-2)$ -Dimensional Edge States of Rotation Symmetry Protected Topological States, *Phys. Rev. Lett.* **119**, 246402 (2017).
- [5] J. Langbehn, Y. Peng, L. Trifunovic, F. von Oppen, and P. W. Brouwer, Reflection-Symmetric Second-Order Topological Insulators and Superconductors, *Phys. Rev. Lett.* **119**, 246401 (2017).
- [6] F. Schindler, A. M. Cook, M. G. Vergniory, Z. Wang, S. S. P. Parkin, B. A. Bernevig, and T. Neupert, Higher-order topological insulators, *Sci. Adv.* **4**, eaat0346 (2018).
- [7] J. Noh, W. A. Benalcazar, S. Huang, M. J. Collins, K. P. Chen, T. L. Hughes, and M. C. Rechtsman, Topological protection of photonic mid-gap defect modes, *Nat. Photonics* **12**, 408 (2018).
- [8] A. E. Hassan, F. K. Kunst, A. Moritz, G. Andler, E. J. Bergholtz, and M. Bourennane, Corner states of light in photonic waveguides, *Nat. Photonics* **13**, 697 (2019).
- [9] S. Mittal, V. V. Orre, G. Zhu, M. A. Gorlach, A. Poddubny, and M. Hafezi, Photonic quadrupole topological phases, *Nat. Photonics* **13**, 692 (2019).
- [10] X.-D. Chen, W.-M. Deng, F.-L. Shi, F.-L. Zhao, M. Chen, and J.-W. Dong, Direct Observation of Corner States in Second-Order Topological Photonic Crystal Slabs, *Phys. Rev. Lett.* **122**, 233902 (2019).
- [11] B.-Y. Xie, G.-X. Su, H.-F. Wang, H. Su, X.-P. Shen, P. Zhan, M.-H. Lu, Z.-L. Wang, and Y.-F. Chen, Visualization of Higher-Order Topological Insulating Phases in Two-Dimensional Dielectric Photonic Crystals, *Phys. Rev. Lett.* **122**, 233903 (2019).
- [12] M. Li, D. Zhirihin, M. Gorlach, X. Ni, D. Filonov, A. Slobozhanyuk, A. Alù, and A. B. Khanikaev, Higher-order topological states in photonic kagome crystals with long-range interactions, *Nat. Photonics* **14**, 89 (2020).
- [13] H. Xue, Y. Yang, F. Gao, Y. Chong, and B. Zhang, Acoustic higher-order topological insulator on a kagome lattice, *Nat. Mater.* **18**, 108 (2019).
- [14] X. Ni, M. Weiner, A. Alù, and A. B. Khanikaev, Observation of higher-order topological acoustic states protected by generalized chiral symmetry, *Nat. Mater.* **18**, 113 (2019).
- [15] Y. Qi, C. Qiu, M. Xiao, H. He, M. Ke, and Z. Liu, Acoustic Realization of Quadrupole Topological Insulators, *Phys. Rev. Lett.* **124**, 206601 (2020).
- [16] Z. Zhang, H. Long, C. Liu, C. Shao, Y. Cheng, X. Liu, and J. Christensen, Deep-subwavelength holey acoustic second-order topological insulators, *Adv. Mater.* **31**, 1904682 (2019).
- [17] X. Zhang, H.-X. Wang, Z.-K. Lin, Y. Tian, B. Xie, M.-H. Lu, Y.-F. Chen, and J.-H. Jiang, Second-order topology and multi-

- dimensional topological transitions in sonic crystals, *Nat. Phys.* **15**, 582 (2019).
- [18] H. Fan, B. Xia, L. Tong, S. Zheng, and D. Yu, Elastic Higher-Order Topological Insulator with Topologically Protected Corner States, *Phys. Rev. Lett.* **122**, 204301 (2019).
- [19] S. Imhof, C. Berger, F. Bayer, J. Brehm, L. W. Molenkamp, T. Kiessling, F. Schindler, C. H. Lee, M. Greiter, T. Neupert, and R. Thomale, Topoelectrical-circuit realization of topological corner modes, *Nat. Phys.* **14**, 925 (2018).
- [20] M. Serra-Garcia, R. Süsstrunk, and S. D. Huber, Observation of quadrupole transitions and edge mode topology in an LC circuit network, *Phys. Rev. B* **99**, 020304(R) (2019).
- [21] H. Yang, Z.-X. Li, Y. Liu, Y. Cao, and P. Yan, Observation of symmetry-protected zero modes in topoelectrical circuits, *Phys. Rev. Research* **2**, 022028(R) (2020).
- [22] L. Song, H. Yang, Y. Cao, and P. Yan, Realization of the square-root higher-order topological insulator in electric circuits, *Nano Lett.* **20**, 7566 (2020).
- [23] M. Z. Hasan and C. L. Kane, Colloquium: Topological insulators, *Rev. Mod. Phys.* **82**, 3045 (2010).
- [24] X.-L. Qi and S.-C. Zhang, Topological insulators and superconductors, *Rev. Mod. Phys.* **83**, 1057 (2011).
- [25] H. Xue, Y. Yang, G. Liu, F. Gao, Y. Chong, and B. Zhang, Realization of an Acoustic Third-Order Topological Insulator, *Phys. Rev. Lett.* **122**, 244301 (2019).
- [26] H. Xue, Y. Ge, H.-X. Sun, Q. Wang, D. Jia, Y.-J. Guan, S.-Q. Yuan, Y. Chong, and B. Zhang, Observation of an acoustic octupole topological insulator, *Nat. Commun.* **11**, 2442 (2020).
- [27] X. Ni, M. Li, M. Weiner, A. Alù, and A. B. Khanikaev, Demonstration of a quantized acoustic octupole topological insulator, *Nat. Commun.* **11**, 2108 (2020).
- [28] J. Bao, D. Zou, W. Zhang, W. He, H. Sun, and X. Zhang, Topoelectrical circuit octupole insulator with topologically protected corner states, *Phys. Rev. B* **100**, 201406(R) (2019).
- [29] X. Zhang, B.-Y. Xie, H.-F. Wang, X. Xu, Y. Tian, J.-H. Jiang, M.-H. Lu, and Y.-F. Chen, Dimensional hierarchy of higher-order topology in three-dimensional sonic crystals, *Nat. Commun.* **10**, 5331 (2019).
- [30] M. Weiner, X. Ni, M. Li, A. Alù, and A. B. Khanikaev, Demonstration of a third-order hierarchy of topological states in a three-dimensional acoustic metamaterial, *Sci. Adv.* **6**, eaay4166 (2020).
- [31] W. Zhang, D. Zou, J. Bao, W. He, Q. Pei, H. Sun, and X. Zhang, Topoelectrical-circuit realization of a four-dimensional hexadecapole insulator, *Phys. Rev. B* **102**, 100102(R) (2020).
- [32] Z.-G. Chen, W. Zhu, Y. Tan, L. Wang, and G. Ma, Acoustic Realization of a Four-Dimensional Higher-Order Chern Insulator and Boundary-Modes Engineering, *Phys. Rev. X* **11**, 011016 (2021).
- [33] L. Zhang, J. Ren, J.-S. Wang, and B. Li, Topological magnon insulator in insulating ferromagnet, *Phys. Rev. B* **87**, 144101 (2013).
- [34] R. Shindou, J.-I. Ohe, R. Matsumoto, S. Murakami, and E. Saitoh, Chiral spin-wave edge modes in dipolar magnetic thin films, *Phys. Rev. B* **87**, 174402 (2013).
- [35] A. Mook, J. Henk, and I. Mertig, Edge states in topological magnon insulators, *Phys. Rev. B* **90**, 024412 (2014).
- [36] R. Chisnell, J. S. Helton, D. E. Freedman, D. K. Singh, R. I. Bewley, D. G. Nocera, and Y. S. Lee, Topological Magnon Bands in a Kagome Lattice Ferromagnet, *Phys. Rev. Lett.* **115**, 147201 (2015).
- [37] X. S. Wang, Y. Su, and X. R. Wang, Topologically protected unidirectional edge spin waves and beam splitter, *Phys. Rev. B* **95**, 014435 (2017).
- [38] A. Rückriegel, A. Brataas, and R. A. Duine, Bulk and edge spin transport in topological magnon insulators, *Phys. Rev. B* **97**, 081106(R) (2018).
- [39] Y. Su and X. R. Wang, Chiral anomaly of Weyl magnons in stacked honeycomb ferromagnets, *Phys. Rev. B* **96**, 104437 (2017).
- [40] Y. Su, X. S. Wang, and X. R. Wang, Magnonic Weyl semimetal and chiral anomaly in pyrochlore ferromagnets, *Phys. Rev. B* **95**, 224403 (2017).
- [41] A. Sil and A. K. Ghosh, First and second order topological phases on ferromagnetic breathing kagome lattice, *J. Phys.: Condens. Matter* **32**, 205601 (2020).
- [42] T. Hirokawa, S. A. Díaz, J. Klinovaja, and D. Loss, Magnonic Quadrupole Topological Insulator in Antiskyrmion Crystals, *Phys. Rev. Lett.* **125**, 207204 (2020).
- [43] A. Mook, S. A. Díaz, J. Klinovaja, and D. Loss, Chiral hinge magnons in second-order topological magnon insulators, [arXiv:2010.04142](https://arxiv.org/abs/2010.04142) [Phys. Rev. B (to be published)].
- [44] M. J. Park, S.-B. Lee, and Y. B. Kim, Hinge magnons from non-collinear magnetic order in honeycomb antiferromagnet, [arXiv:2103.01919](https://arxiv.org/abs/2103.01919).
- [45] A. Wachowiak, J. Wiebe, M. Bode, O. Pietzsch, M. Morgenstern, and R. Wiesendanger, Direct observation of internal spin structure of magnetic vortex cores, *Science* **298**, 577 (2002).
- [46] I. Makhfudz, B. Krüger, and O. Tchernyshyov, Inertia and Chiral Edge Modes of a Skyrmion Magnetic Bubble, *Phys. Rev. Lett.* **109**, 217201 (2012).
- [47] S. Mühlbauer, B. Binz, F. Jonietz, C. Pfleiderer, A. Rosch, A. Neubauer, R. Georgii, and P. Böni, Skyrmion lattice in a chiral magnet, *Science* **323**, 915 (2009).
- [48] W. Jiang, P. Upadhyaya, W. Zhang, G. Yu, M. B. Jungfleisch, F. Y. Fradin, J. E. Pearson, Y. Tserkovnyak, K. L. Wang, O. Heinonen, S. G. E. te Velthuis, and A. Hoffmann, Blowing magnetic skyrmion bubbles, *Science* **349**, 283 (2015).
- [49] G. Catalan, J. Seidel, R. Ramesh, and J. F. Scott, Domain wall nanoelectronics, *Rev. Mod. Phys.* **84**, 119 (2012).
- [50] S. K. Kim and Y. Tserkovnyak, Chiral Edge Mode in the Coupled Dynamics of Magnetic Solitons in a Honeycomb Lattice, *Phys. Rev. Lett.* **119**, 077204 (2017).
- [51] Z.-X. Li, C. Wang, Y. Cao, and P. Yan, Edge states in a two-dimensional honeycomb lattice of massive magnetic skyrmions, *Phys. Rev. B* **98**, 180407(R) (2018).
- [52] W. P. Su, J. R. Schrieffer, and A. J. Heeger, Solitons in Polyacetylene, *Phys. Rev. Lett.* **42**, 1698 (1979).
- [53] Z.-X. Li, Z. Wang, Y. Cao, H. W. Zhang, and P. Yan, Robust edge states in magnetic soliton racetrack, *Phys. Rev. B* **103**, 054438 (2021).
- [54] G. Go, I.-S. Hong, S.-W. Lee, S. K. Kim, and K.-J. Lee, Realization of Su-Schrieffer-Heeger states based on metamaterials of magnetic solitons, *Phys. Rev. B* **101**, 134423 (2020).
- [55] Z.-X. Li, Y. Cao, P. Yan, and X. R. Wang, Higher-order topological solitonic insulators, *npj Comput. Mater.* **5**, 107 (2019).



- [56] Z.-X. Li, Y. Cao, X. R. Wang, and P. Yan, Symmetry-Protected Zero Modes in Metamaterials Based on Topological Spin Texture, *Phys. Rev. Appl.* **13**, 064058 (2020).
- [57] Z.-X. Li, Y. Cao, X. R. Wang, and P. Yan, Second-order topological solitonic insulator in a breathing square lattice of magnetic vortices, *Phys. Rev. B* **101**, 184404 (2020).
- [58] Z.-X. Li, Y. Cao, and P. Yan, Topological insulators and semimetals in classical magnetic systems, *Phys. Rep.* **915**, 1 (2021).
- [59] Y. Guang, I. Bykova, Y. Liu, G. Yu, E. Goering, M. Weigand, J. Gräfe, S. K. Kim, J. Zhang, H. Zhang, Z. Yan, C. Wan, J. Feng, X. Wang, C. Guo, H. Wei, Y. Peng, Y. Tserkovnyak, X. Han, and G. Schutz, Creating zero-field skyrmions in exchange-biased multilayers through X-ray illumination, *Nat. Commun.* **11**, 949 (2020).
- [60] M. Hänze, C. F. Adolff, B. Schulte, J. Möller, M. Weigand, and G. Meier, Collective modes in three-dimensional magnonic vortex crystals, *Sci. Rep.* **6**, 22402 (2016).
- [61] M. Möller, J. H. Gaida, S. Schäfer, and C. Ropers, Few-nm tracking of current-driven magnetic vortex orbits using ultrafast Lorentz microscopy, *Commun. Phys.* **3**, 36 (2020).
- [62] A. A. Thiele, Steady-State Motion of Magnetic Domains, *Phys. Rev. Lett.* **30**, 230 (1973).
- [63] J. Shibata, K. Shigetani, and Y. Otani, Dynamics of magnetostatically coupled vortices in magnetic nanodisks, *Phys. Rev. B* **67**, 224404 (2003).
- [64] J. Shibata and Y. Otani, Magnetic vortex dynamics in a two-dimensional square lattice of ferromagnetic nanodisks, *Phys. Rev. B* **70**, 012404 (2004).
- [65] K. Yu. Guslienko, K. S. Buchanan, S. D. Bader, and V. Novosad, Dynamics of coupled vortices in layered magnetic nanodots, *Appl. Phys. Lett.* **86**, 223112 (2005).
- [66] M. W. Yoo, J. Lee, and S. K. Kim, Radial-spin-wave-mode-assisted vortex-core magnetization reversals, *Appl. Phys. Lett.* **100**, 172413 (2012).
- [67] S. Velten, R. Streubel, A. Farhan, N. Kent, M.-Y. Im, A. Scholl, S. Dhuey, C. Behncke, G. Meier, and P. Fischer, Vortex circulation patterns in planar microdisk arrays, *Appl. Phys. Lett.* **110**, 262406 (2017).
- [68] A. Vansteenkiste, J. Leliaert, M. Dvornik, M. Helsen, F. Garcia-Sanchez, and B. V. Waeyenberge, The design and verification of MuMax3, *AIP Adv.* **4**, 107133 (2014).
- [69] S. S. Cherepov, B. C. Koop, A. Yu. Galkin, R. S. Khymyn, B. A. Ivanov, D. C. Worledge, and V. Korenivski, Core-Core Dynamics in Spin Vortex Pairs, *Phys. Rev. Lett.* **109**, 097204 (2012).
- [70] A. V. Bondarenko, E. Holmgren, Z. W. Li, B. A. Ivanov, and V. Korenivski, Chaotic dynamics in spin-vortex pairs, *Phys. Rev. B* **99**, 054402 (2019).
- [71] A. V. Chumak, A. A. Serga, and B. Hillebrands, Magnon transistor for all-magnon data processing, *Nat. Commun.* **5**, 4700 (2014).
- [72] V. V. Kruglyak, S. O. Demokritov, and D. Grundler, Magnonics, *J. Phys. D* **43**, 264001 (2010).
- [73] A. V. Chumak, V. I. Vasyuchka, A. A. Serga, and B. Hillebrands, Magnon spintronics, *Nat. Phys.* **11**, 453 (2015).
- [74] B. Lenk, H. Ulrichs, F. Garbs, and M. Münzenberg, The building blocks of magnonics, *Phys. Rep.* **507**, 107 (2011).
- [75] A. A. Serga, A. V. Chumak, and B. Hillebrands, YIG magnonics, *J. Phys. D* **43**, 264002 (2010).
- [76] J. Lan, W. Yu, R. Wu, and J. Xiao, Spin-Wave Diode, *Phys. Rev. X* **5**, 041049 (2015).
- [77] F. Garcia-Sanchez, P. Borys, R. Soucaille, J.-P. Adam, R. L. Stamps, and J.-V. Kim, Narrow Magnonic Waveguides Based on Domain Walls, *Phys. Rev. Lett.* **114**, 247206 (2015).
- [78] K. Wagner, A. Kákay, K. Schultheiss, A. Henschke, T. Sebastian, and H. Schultheiss, Magnetic domain walls as reconfigurable spin-wave nanochannels, *Nat. Nanotechnol.* **11**, 432 (2016).